Latent Electronic (Anti-)Ferroelectricity in BiNiO₃

Subhadeep Bandyopadhyay[*] and Philippe Ghosez[†]

Theoretical Materials Physics, Q-MAT, Université de Liège, B-4000 Sart-Tilman, Belgium

BiNiO₃ exhibits an unusual metal-insulator transition from $Pnma$ to $P\bar{1}$ that is related to charge ordering at the Bi sites, which is intriguingly distinct from the charge ordering at Ni sites usually observed in related rare-earth nickelates. Here, using first principles calculations, we first rationalize the phase transition from $Pnma$ to $P\bar{1}$, revealing an overlooked intermediate $P2_1/m$ bridging phase and a complex interplay between distinct degrees of freedom. Going further, we point out that the charge ordering at Bi sites in the $P\bar{1}$ phase is not unique. We highlight an alternative polar ordering giving rise to a ferroelectric $Pmn2_1$ phase nearly degenerated in energy with $P\bar{1}$ and showing an in-plane electric polarization of 53 μC/cm² directly resulting from the charge ordering. The close energy of $Pmn2_1$ and $P\bar{1}$ phases, together with low energy barrier between them, make BiNiO₃ a potential electronic antiferroelectric in which the field-induced transition from nonpolar to polar would relate to nonadiabatic intersite electron transfer. We also demonstrate the possibility to stabilize an electronic ferroelectric ground state from strain engineering in thin films, using an appropriate substrate.

Nickelate perovskites (RNiO₃ with R = Y or a rare-earth element) have generated a significant interest over the last years due to their fascinating electronic, magnetic, and structural properties, potentially linked to a wide variety of functional applications [1,2]. RNiO₃ compounds (except R = La) undergo a metal to insulator transition (MIT) with associated structural phase transition from high-temperature orthorhombic $Pnma$ to low-temperature monoclinic $P2_1/n$ structure [3]. The critical temperature of the MIT decreases with increasing R^{3+} ionic radius and is finally suppressed for LaNiO₃, which exhibits a distinct metallic $R\bar{3}c$ phase at all temperatures. For smaller R^{3+} ion, the MIT is driven by a breathing distortion of the NiO₆ octahedra, which creates two inequivalent Ni sites and subsequent charge ordering (CO), $2Ni^{3+} \rightarrow Ni^{2+} + Ni^{4+}$ [4,5]. At the electronic level, considering Ni-O hybridizations, this formal transition is often better reformulated in terms of oxygen holes ($\underline{L}$): $2(Ni^{2+}\underline{L}^1) \rightarrow Ni^{2+} + Ni^{2+}\underline{L}^2$ [6,7]. At the structural level, it has been shown that the breathing distortion is triggered by the oxygen octahedra rotations (OOR) inherent to the $Pnma$ phase [8]. This behavior is ubiquitous among the RNiO₃ compounds, making them a distinct and well-defined family of materials.

We might naturally expect BiNiO₃ to belong to this class of compounds. In view of the similar size of Bi³⁺ and La³⁺ cations, it is questionable why BiNiO₃ does not behave like LaNiO₃ [9,10]. However, relying instead on bond-valence analysis [11], it appears that BiNiO₃ has a Goldschmidt

tolerance factor [12] very similar to SmNiO₃ [see Supplemental Material (SM) Fig. S1(a)] [13]. In line with that, BiNiO₃ shows a metallic $Pnma$ phase with OOR amplitudes comparable to those of SmNiO₃ (see SM). Like the latter, it then exhibits an insulating ground state but instead of crystallizing in the same insulating $P2_1/n$ phase with CO at the Ni sites, it is reported in an unusual $P\bar{1}$ phase combining an unexpected Ni²⁺ state with CO at the Bi sites (Bi³⁺Ni³⁺ → $Bi^{3+}_{1/2}Bi^{5+}_{1/2}Ni^{2+}$) [26,27]. Although the $P2_1/n$ phase has been theoretically predicted to be metastable [28], it has never been experimentally observed. A temperature versus pressure phase diagram has been reported experimentally, suggesting direct phase transition from $Pnma$ to $P\bar{1}$ at a critical temperature decreasing linearly with increasing pressure [29].

Various studies have discussed the MIT in BiNiO₃, focusing mainly on the electronic properties. Dynamical mean field theory calculations [30–32] reproduce CO of Bi³⁺ and Bi⁵⁺ in the insulating phase assuming Bi⁴⁺ to be a valence skipper with an attractive Hubbard interaction, while the formal Bi³⁺Ni³⁺ occupancy makes BiNiO₃ a metal in the $Pnma$ phase. This integer valence description is too simple to reflect the exact electronic configurations and x-ray absorption spectroscopy finds a charge state away from Ni³⁺ [33] in the metallic state. Paul *et al.* [34] then better proposed an description of the form $(Bi^{3+}\underline{L}^{\delta})(Ni^{2+}\underline{L}^{1-\delta}) \rightarrow Bi^{3+}_{1/2}(Bi^{3+}\underline{L}^{2(1-\delta)})_{1/2}(Ni^{2+}\underline{L}^{\delta})$ involving oxygen holes $\underline{L}$ and explained the pressure dependence of the MIT from changes of Bi-O and Ni-O hybridizations. Hereafter, reported charge states refer to the

---
[*]Contact author: subha.7491@gmail.com
[†]Contact author: Philippe.Ghosez@uliege.be

nominal oxidation state, while it must be understood that the actual atomic charge can deviate from it due to the formation of oxygen holes (e.g., $Bi^{5+} \approx Bi^{3+}\underline{L}^2$) [35].

Here, we report a detailed first-principles study of $BiNiO_3$ addressing together electronic and structural aspects. Our approach accurately reproduces the CO and $P\bar{1}$ ground state. First, we unveil the existence of an intermediate $P2_1/m$ bridging phase along the path from the high-temperature $Pnma$ phase to the $P\bar{1}$ ground state and complex interplay between distinct stable distortions to lower the energy from $P2_1/m$ to $P\bar{1}$. Then, we point out that the CO of the $P\bar{1}$ phase is not unique and identify an alternative CO giving rise to a ferroelectric $Pmn2_1$ phase of comparable energy. We clarify that ferroelectricity in that phase is electronic in nature and discuss practical implication of our findings in terms of electronic (anti-) ferroelectricity.

Our calculations are performed using a density-functional theory with the Hubbard U parameter (DFT + U) approach, relying on the PBEsol [36] exchange-correlation functional, as implemented in ABINIT software [37–39] (see SM). U and J corrections are included for Ni $3d$ states [40]. We checked the results for different (U, J) values and found that (6,1) eV provides an excellent theoretical description of the experimental $P\bar{1}$ ground state [Fig. 1(a) and see SM, Table S1]. For too small U, $P\bar{1}$ cannot be stabilized, consistently with Ref. [28]. Atomic distortions are
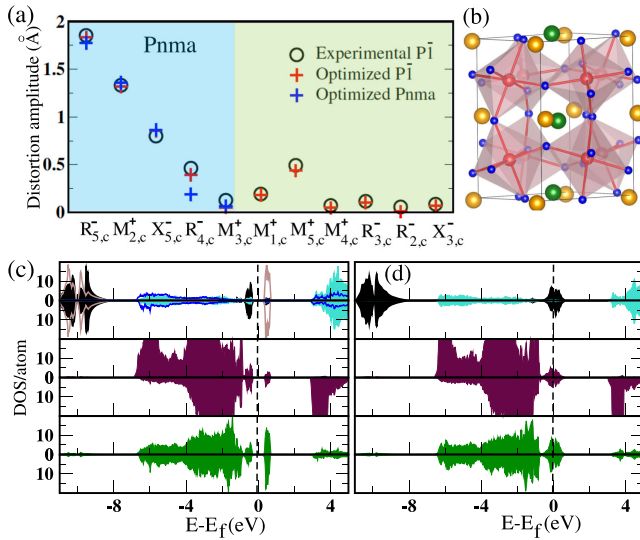

FIG. 1. (a) Symmetry-adapted mode analysis of the atomic distortion, with respect to the cubic phase, in the experimental (open circle) [44] and optimized (red +) $P\bar{1}$ structures and in the optimized (blue +) $Pnma$ phase. (b) Sketch of the $P\bar{1}$ crystal structure, with $Bi_S = Bi^{5+}$ (green), $Bi_L = Bi^{3+}$ (orange), Ni (red), and O (blue) atoms. Partial DOS of (c) $P\bar{1}$ and (d) $Pnma$ phases, highlighting Bi_L $6s$ (black), Bi_S $6s$, (brown line), Bi_L $6p$ (cyan), Bi_S $6p$ (blue line), Ni $3d$ (maroon), O $2p$ (green) contributions. Vertical dashed line locates E_f.

described from symmetry-adapted mode analysis using ISODISTORT [41]. Below, a subscript is added to symmetry-adapted mode labels to specify to which phase they refer: c for cubic ($Pm\bar{3}m$), o for orthorhombic ($Pnma$), and m for monoclinic ($P2_1/m$). Connection between symmetry labels of the three phases is reported in Table S3 [13]. Such an approach is generic and relevant to analyze first- and second-order transitions [8,42]. Nonadiabatic charge transfer is probed using constrained DFT, as implemented in ABINIT [43].

$P\bar{1}$ *ground state*—Starting from the experimental $P\bar{1}$ structure, we first carry out full structural optimization for different collinear magnetic configurations of Ni. Comparing ferromagnetic (FM) with A, C, G, S, E, and T type antiferromagnetic (AFM) spin orders, we find G-AFM to be energetically the most favorable order (Table S2 [13]), with a theoretical unit cell volume (233 Å³) comparable to experiment (233–235 Å³) [27,29]. Since G-AFM spin configuration also remains the most favorable in other phases, it is kept all along this work.

The atomic structure of the $P\bar{1}$ phase is characterized by quantifying, from symmetry-adapted mode analysis [41], the atomic distortions with respect to the cubic perovskite $Pm\bar{3}m$ parent phase, which although not observed experimentally constitutes a well-defined and valuable reference (see SM [13]). Figure 1(a) points out the excellent agreement between the experimental [44] and optimized theoretical structures. Among the dominant distortions, some are already inherent to the intermediate $Pnma$ phase [8,45]: primary in-phase ($M_{2,c}^+$) and antiphase ($R_{5,c}^-$) NiO_6 octahedra rotations together with secondary antipolar motions of Bi atoms ($X_{5,c}^-$ and $R_{4,c}^-$) and more negligible Jahn-Teller distortion ($M_{3,c}^+$). Then, additional $M_{1,c}^+$ and $M_{5,c}^+$ distortions (Fig. S3 [13]) are also present, which explain together the lowering of symmetry from $Pnma$ to $P\bar{1}$: $M_{1,c}^+$ motions of O atoms in the ab plane, which induce a breathinglike distortion of BiO_{12} polyhedra and $M_{5,c}^+$ antiphase motions of O atoms along c, which distort the polyhedra further. This gives rise to large (Bi_L, 51.07 Å³) and small (Bi_S, 47.24 Å³) Bi sites that order according to a C-type pattern in which Bi_L and Bi_S alternate along two directions and are preserved in the third one [Fig. 1(b)]. Small $R_{3,c}^-$, $M_{4,c}^+$, and $X_{3,c}^-$ distortions are also present. The negligible contribution of the $R_{2,c}^-$ mode confirms the absence of breathing distortion at Ni sites, dominant in the insulating $P2_1/n$ phase of other $RNiO_3$ perovskites [5,8].

The partial density of states (PDOS) in Fig. 1(c) reveal dominant antibonding $Bi\,6s + O\,2p$ contributions around the Fermi energy (E_f), whereas bonding states are lying much deeper (i.e., ~10 eV below E_f). In the $P\bar{1}$ phase, a splitting between antibonding $Bi\,6s + O\,2p$ states is opening a band gap of 0.5 eV in line with experiment [46]. Distinct Bi_L and Bi_S contributions with occupied
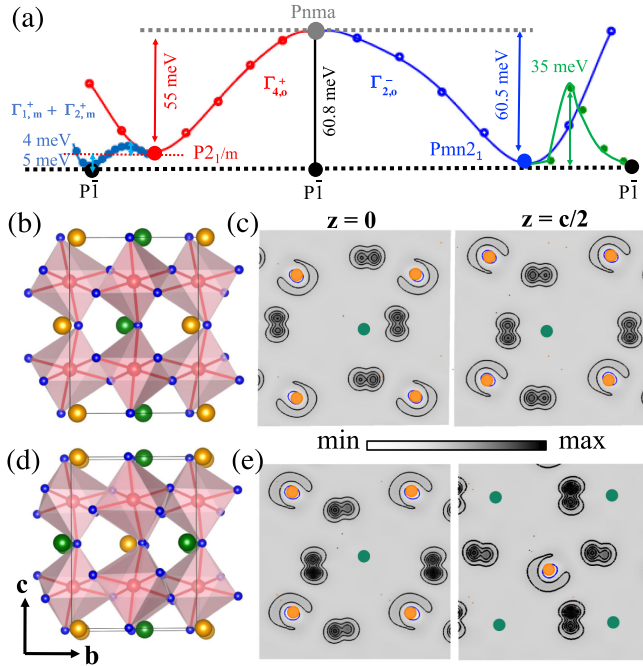
FIG. 2. (a) Energy landscape of BiNiO$_3$, locating the different phases and the energy barriers between them (G-type AFM spin ordering). Crystal structure and partial charge density of top valence electrons (b),(c) in the $P2_1/m$ and $P\bar{1}$ phases and (d),(e) in the $Pmn2_1$ phase.

(unoccupied) $6s$ levels near E_f are consistent with Bi^{3+} and Bi^{5+} (or Bi$^{3+}\underline{L}^2$) states, giving rise to CO according to a C-type pattern [34]. This is confirmed by charge density plots of top valence electrons [Fig. 2(c), Fig. S4a], highlighting the presence of a Bi $6s$ lone pairs at the Bi$_L$ site only. These lone pairs are pointing along the pseudocubic diagonal in each ab plane; they are lying on the same side of Bi atoms in a given ab plane and in opposite sides in consecutive layers, in line with antipolar motion of Bi atoms and inversion symmetry of the system.

Also, PDOS of the Ni $3d$ show that t_{2g} states are occupied for both the spin channel and e_g states are occupied (empty) for majority (minority) spin channel. This confirms a high-spin Ni$^{2+}(t_{2g}^6 e_g^2)$ state, consistent with the calculated magnetic moment of $\sim 1.67~\mu_B$/Ni. Small differences in the Ni magnetic moments results in an uncompensated ferrimagnetic (FiM) net magnetization of 0.01 μ_B. Such a weak magnetization is also observed experimentally, but as a result of a canted G-AFM ordering [44].

Pnma phase—The $Pnma$ phase lies 61 meV/f.u. higher in energy than $P\bar{1}$. Its relaxed unit cell volume (228 Å^3) is $\sim 2.4\%$ smaller than that of $P\bar{1}$, consistently with the $\sim 2.5\%$ volume shrinkage observed experimentally during the $P\bar{1}$-$Pnma$ transition at 3.5 GPa [29]. Structurally, the $Pnma$ phase ($a^-b^+a^-$ in Glazer's notations) shows large out-of-phase and in-phase NiO$_6$ octahedra rotations of 9.6° and 11.2°, which remain similar in the $P\bar{1}$ phase [Fig. 1(b)].

At the electronic level, the PDOS [Fig. 1(d)] point out a metallic character, with partially occupied Bi $6s$ and O $2p$ antibonding states at E_f. The significant occupancy of Ni $3d$ states and the Ni magnetic moment of 1.65 μ_B indicate a charge state closer to high-spin Ni^{+2} than to Ni^{+3}, in line with experimental observations [33]. Consequently, the nominal charge state of Bi should be Bi^{4+}, which suggests a strong tendency to electronic instability since Bi^{4+} is a valence skipper [47]. Accordingly, the $Pnma$ phase shows two unstable phonon modes at Γ: a $\Gamma_{4,o}^+$ (310i cm^{-1}) and a $\Gamma_{2,o}^-$ mode (149i cm^{-1}) that both induce CO at Bi sites.

Condensing the $\Gamma_{4,o}^+$ mode lowers the symmetry to $P2_1/m$ and gives rise to a relaxed insulating metastable phase located 55 meV/f.u. below the $Pnma$ phase [Fig. 2(a)]. Inspection of the PDOS highlights a band gap of 0.46 eV and confirms charge disproportionation at the Bi sites (Fig. S5). This $P2_1/m$ phase shows a C-type CO and lone-pair orientations similar to $P\bar{1}$ [Figs. 2(b)–2(c)].

Condensing instead the $\Gamma_{2,o}^-$ mode lowers the symmetry to $Pmn2_1$ and gives rise to another insulating metastable phase located 60.5 meV/f.u. below the $Pnma$ phase (i.e., only 0.3 meV/f.u. above $P\bar{1}$). Inspection of the PDOS also show charge disproportionation at the Bi sites (shown in Fig. S5) but Bi$_S$ $6s$ states are much broaden at the conduction level (compared to $P2_1/m$ and $P\bar{1}$), indicating stronger Bi $6s$–O $2p$ hybridizations resulting in a smaller band gap of 0.3 eV. Moreover, Bi^{3+} and Bi^{5+} sites now alternate along the three directions giving rise to a G-type CO that breaks the inversion symmetry in line with the polar character of the $Pmn2_1$ phase.

Interestingly, the only appearance of C-type (respectively, G-type) CO in $Pnma$ already lowers the symmetry to $P2_1/m$ (respectively, $Pmn2_1$). Together with the close energies of $Pmn2_1$, $P2_1/m$, and $P\bar{1}$ phases, this emphasizes that the major driving force destabilizing the $Pnma$ structure is CO, whatever the resulting order.

Path to the ground state—Amazingly, the $P2_1/m$ and $Pmn2_1$ phases are both dynamically stable. The natural path from $Pnma$ to $P\bar{1}$ should preferably go through $P2_1/m$, which already condense $\Gamma_{4,o}^+$ distortion. In the monoclinic $P2_1/m$ phase, none of the mode is, however, unstable but additional condensation of the low frequency $\Gamma_{2,m}^+$ mode (50 cm^{-1}) properly brings the system to the $P\bar{1}$ ground state. Doing so requires, however, overcoming an energy barrier of 4 meV/f.u.

In order to clarify the mechanism of this unusual phase transition condensing a stable mode, we studied the energy landscape around the $P2_1/m$ phase from a Landau-type expansion (up to 4th order, Eq. S1 [13]) involving $\Gamma_{2,m}^+ = \Gamma_{3,o}^+ \oplus \Gamma_{2,o}^+$ and $\Gamma_{1,m}^+ = \Gamma_{1,o}^+ \oplus \Gamma_{4,o}^+$ lattice modes as well as $\eta_{\Gamma_{1,m}^+}$ and $\eta_{\Gamma_{2,m}^+}$ macroscopic strains degrees of freedom. The coefficients have been adjusted on a training set of DFT data including 300 configurations (Fig. S6 and are reported in Table S5 [13]). Among the

coupling terms, the 3rd order coupling $Q_{\Gamma_{1,m}^+} Q_{\Gamma_{2,m}^+}^2$ is the most significant in lowering the energy (-456 meV/f.u.). Then, strain couplings $Q_{\Gamma_{2,m}^+} \eta_{\Gamma_{2,m}^+}$ (-100 meV/f.u.) and $Q_{\Gamma_{2,m}^+}^2 \eta_{\Gamma_{1,m}^+}$ (-232 meV/f.u.) are also significant.

This analysis of the energy landscape at zero kelvin reveals that reaching the $P\bar{1}$ ground state requires the cooperative coupling of distinct degrees of freedom, which is compatible with the observed first-order character of the transition [29]. Further description of the phase transition at finite temperature is appealing but would require molecular dynamics simulations, which remain challenging at the DFT level and might better call for a second-principles approach [48].

Competing polar phase and electronic ferroelectricity— Being only 0.3 meV/f.u. higher in energy than the observed $P\bar{1}$ ground state, the $Pmn2_1$ phase emerges as a close and competing phase. As previously discussed, its G-type CO (Fig. 3) phase breaks inversion symmetry, yielding a spontaneous polarization along x, P_x^s.

Estimating P_x^s is not so trivial. Berry-phase calculation in the $Pmn2_1$ phase delivers a set of values $P_x^s = -20.52 + nQ_P$ μC/cm^2 (with n an integer and $Q_P = 36.76$ μC/cm^2 the polarization quantum), without clarifying which value of n is appropriate. Using a nudged elastic band (NEB) technique, we identified an insulating low-energy path from nonpolar $P\bar{1}$ to polar $Pmn2_1$ phase [with an energy barrier of 35 meV/f.u., Fig. 2(a)]. From this, we can follow the

FIG. 3. (a) Evolution of P_x^s along the insulating NEB path from $P\bar{1}$ ($\lambda = 0$) to $Pmn2_1$ ($\lambda = 1$), with CO evolving from C type (red dots) to G type (green dots). P_y^s (blue dots) remains negligible along the path. (b) Evolution of Bi $6s$ PDOS at selected points along the NEB path as defined in (c). Black and brown correspond to Bi_L and Bi_s in $P\bar{1}$, which switches their character gradually. (c) Evolution of the energy along the NEB path connecting $P\bar{1}$ ($\lambda = 0$) to $Pmn2_1$ with $+P_x^s$ ($\lambda = 1$) and $-P_x^s$ ($\lambda = -1$): adiabatic path (black dots), nonadiabatic paths with atomic structure at $\lambda = 0$ (red dots) and $\lambda = +1$ (green dots) [54].

evolution of P_x^s along the path, as illustrated in Fig. 3(a). This shows first that the spontaneous polarization of the $Pmn2_1$ phase is $P_x^s = 53$ μC/cm^2, which is even larger than that of a conventional ferroelectric like BaTiO$_3$. Then, it clarifies that the change of polarization is strongly nonlinear with a jump of about 40 μC/cm^2. This jump that can be assigned to the change from C-type to G-type CO as highlighted from the PDOS of Bi in Fig. 3(b). It is also compatible (see SM) with the transfer of two electrons between Bi sites in one layer [$z = 1/2$ in Fig. 2(b)], confirming that P_x^s mainly originates from electronic CO.

Further, the direction of P_x^s can be reversed by reversing the charge ordering (i.e., condensing $\Gamma_{2,o}^-$ in the opposite direction), which makes the $Pmn2_1$ phase a conceptual electronic ferroelectric phase. A possible path for switching the polarization is going through the $P\bar{1}$ phase [Fig. 3(c)], which offers a lower energy barrier with respect to a linear interpolation between oppositely polarized $Pmn2_1$ phases (energy barrier of ~ 60 meV/f.u.).

Following Rabe [49], the nonpolar character of the $P\bar{1}$ ground state, combined with the very close energy of the $Pmn2_1$ ferroelectric phase ($\Delta E = 0.3$ meV/f.u.), makes BiNiO$_3$ a potential antiferroelectric, as long as a nonpolar to ferroelectric transition can be achieved under an accessible external electric field. Applying an electric field $\mathcal{E}_T = \Delta E / \Omega_0 P_x^s \approx 15$ kV/cm should be enough to stabilize thermodynamically $Pmn2_1$ against the $P\bar{1}$ phase [50]. However, achieving the field-induced transition would *a priori* require a much larger field $\mathcal{E}_A$ to overcome the adiabatic energy barrier between the two phases ($\Delta E_A \approx 35$ meV/f.u. at zero field and zero kelvin). Alternatively, it might be questioned if nonadiabatic electron transfer would eventually be possible. Following the scheme proposed Qi and Rabe [51] [see Fig. 3(c) and SM [13]], we estimate the field required for nonadiabatic transition to $\mathcal{E}_{NA} = \Delta E_{NA} / \Omega_0 P_x^s \approx 800$ kV/cm ($\Delta E_{NA} = 15$ meV/f.u.). As discussed by Qi and Rabe, this should not be taken as an exact value but rather as an estimate to compare distinct compounds. Our computed $\mathcal{E}_{NA}$ is larger than that reported in Fe$_3$O$_4$ [51,52] showing a similar band gap and in which ferroelectric switching has been experimentally observed [53]. It is, however, significantly smaller than in other electronic ferroelectrics like SrVO$_3$/LaVO$_3$ or LuFe$_2$O$_4$ [51]. As such, BiNiO$_3$ remains a plausible candidate for electronic antiferroelectricity, with field induced nonpolar to polar transition potentially accessible and driven by nonadiabatic electron transfer.

Strain engineering—Interestingly, the lattice parameters (along a and c) of the $Pmn2_1$ phase are significantly different from those of the $P\bar{1}$ ground state (see Table S7 [13]), which opens the perspective of using strain engineering to stabilize a ferroelectric ground state. It appears that the lattice parameters of the NdGaO$_3$, a widely used substrate for the growth of perovskite oxide films, perfectly match with those of the $Pmn2_1$ phase. Comparing then the
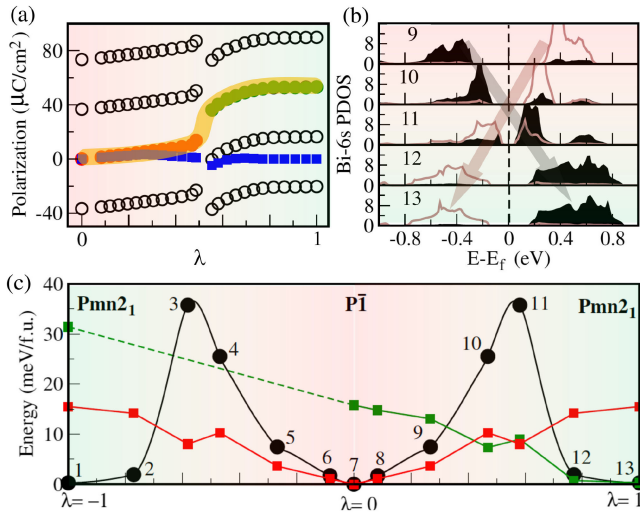
energies of different possible orientations of $P\bar{1}$ and $Pmn2_1$ phases, epitaxially strained on commercially available $(001)_o$ and $(110)_o$ NdGaO$_3$ substrates (Tables S8 and S9 [13]), it appears that the ferroelectric $Pmn2_1$ phase is always elastically favored. In the case of the $(110)_o$ substrate, the strained $Pmn2_1$ ferroelectric phase lies 7 meV/f.u. below the strained $P\bar{1}$ and moreover aligns its long axis in plane as that of the substrate, which makes it a likely case to be realized experimentally. Polarization switching in such a marginally strained polar $Pmn2_1$ phase would require reversing the CO and as such electron transfer in each of the two layers [$z = 0$ and $1/2$ of Fig. 2(d)]. According to Fig. 3(c), it should be accessible from nonadiabatic electron transfer at the same reasonable field $\mathcal{E}_{NA} \approx 800$ kV/cm as before, making the system a potential electronic ferroelectric. Being a weak ferromagnet, it would be *de facto* multiferroic [55].

Conclusions—BiNiO$_3$ behaves differently from other nickelate perovskites and shows CO at Bi rather than Ni sites. In the metallic $Pnma$ phase, Ni adopts an oxidation state close to Ni^{2+} which tends to promote Bi^{4+}. The latter being a valence skipper state, the $Pnma$ phase is unstable with respect to CO at Bi sites, which explains both the transition to the insulating nonpolar $P\bar{1}$ ground state and the presence of the close ferroelectric $Pmn2_1$ phase. TlMnO$_3$ [56] is another alternative perovskite we found hosting a $P\bar{1}$ ground state. Interestingly, it also shows a metallic $Pnma$ to insulating $P\bar{1}$ phase transition but coming instead from orbital ordering at Mn^{3+} sites. We want to stress that ferroelectricity in BiNiO$_3$ is distinct from that in other BiMO$_3$ perovskites (M = Fe, Co, In) [57–59] in which only Bi^{3+} is present and polarization driven by the lone pair of Bi^{3+}. In BiNiO$_3$, the polarization arises from the G-type Bi^{3+}/Bi^{5+} CO and is electronic in nature. Electronic ferroelectricity has been reported in non-perovskite Fe$_3$O$_4$ [52], AFe$_2$O$_4$ compounds [60,61] and perovskite oxide superlattices [62,63] but remains a rare phenomena. Stabilizing the polar $Pmn2_1$ phase of BiNiO$_3$ by electric field or strain engineering appears as a promising new platform to probe further the intriguing concept of electronic (anti-)ferroelectricity.

[1] Y. Zhou, X. Guan, H. Zhou, K. Ramadoss, S. Adam, H. Liu, S. Lee, J. Shi, M. Tsuchiya, D. D. Fong, and S. Ramanathan, Nature (London) **534**, 231 (2016).

[2] J. Shi, S. D. Ha, Y. Zhou, F. Schoofs, and S. Ramanathan, Nat. Commun. **4**, 2676 (2013).

[3] J. A. Alonso, M. J. Martnez-Lope, M. T. Casais, M. A. G. Aranda, and M. T. Fernndez-Daz, J. Am. Chem. Soc. **121**, 4754 (1999).

[4] I. I. Mazin, D. I. Khomskii, R. Lengsdorf, J. A. Alonso, W. G. Marshall, R. M. Ibberson, A. Podlesnyak, M. J. Martínez-Lope, and M. M. Abd-Elmeguid, Phys. Rev. Lett. **98**, 176406 (2007).

[5] J. Varignon, M. N. Grisolia, J. Íñiguez, A. Barthélémy, and M. Bibes, npj Quantum Mater. **2**, 21 (2017).

[6] S. Johnston, A. Mukherjee, I. Elfimov, M. Berciu, and G. A. Sawatzky, Phys. Rev. Lett. **112**, 106404 (2014).

[7] V. Bisogni, S. Catalano, R. J. Green, M. Gibert, R. Scherwitzl, Y. Huang, V. N. Strocov, P. Zubko, S. Balandeh, J.-M. Triscone, G. Sawatzky, and T. Schmitt, Nat. Commun. **7**, 13017 (2016).

[8] A. Mercy, J. Bieder, J. Íñiguez, and P. Ghosez, Nat. Commun. **8**, 1677 (2017).

[9] R. D. Shannon, Acta Crystallogr. A **32**, 751 (1976).

[10] M. Lufaso, https://lufaso.domains.unf.edu/spuds/radii-alpha.pdf.

[11] N. E. Brese and M. O'Keeffe, Acta Crystallogr. Sect. B **47**, 192 (1991).

[12] V. M. Goldschmidt, Naturwissenschaften **14**, 477 (1926).

[13] See Supplemental Material at http://link.aps.org/supplemental/10.1103/PhysRevLett.133.146801 for further information, which includes Refs. [14–25].

[14] P. Hohenberg and W. Kohn, Phys. Rev. **136**, B864 (1964).

[15] W. Kohn and L. J. Sham, Phys. Rev. **140**, A1133 (1965).

[16] P. E. Blöchl, Phys. Rev. B **50**, 17953 (1994).

[17] X. Gonze *et al.*, Comput. Phys. Commun. **180**, 2582 (2009).

[18] S. Baroni, S. de Gironcoli, A. Dal Corso, and P. Giannozzi, Rev. Mod. Phys. **73**, 515 (2001).

[19] G. Henkelman and H. Jnsson, J. Chem. Phys. **113**, 9978 (2000).

[20] B. J. Campbell, H. T. Stokes, D. E. Tanner, and D. M. Hatch, J. Appl. Crystallogr. **39**, 607 (2006).

[21] G. Kresse and J. Hafner, Phys. Rev. B **47**, 558 (1993).

G. Kresse and J. Furthmller, Comput. Mater. Sci. **6**, 15 (1996).

G. Kresse and J. Furthmüller, Phys. Rev. B **54**, 11169 (1996).

[24] G. Kresse and D. Joubert, Phys. Rev. B **59**, 1758 (1999).

[25] *Mathematica*, https://www.wolfram.com/mathematica/.

[26] S. Ishiwata, M. Azuma, M. Takano, E. Nishibori, M. Takata, M. Sakata, and K. Kato, J. Mater. Chem. **12**, 3733 (2002).

[27] M. Azuma, S. Carlsson, J. Rodgers, M. G. Tucker, M. Tsujimoto, S. Ishiwata, S. Isoda, Y. Shimakawa, M. Takano, and J. P. Attfield, J. Am. Chem. Soc. **129**, 14433 (2007).

[28] N. Cohen and O. Diéguez, Phys. Rev. B **104**, 064111 (2021).

[29] M. Azuma, W.-t. Chen, H. Seki, M. Czapski, S. Olga, K. Oka, M. Mizumaki, T. Watanuki, N. Ishimatsu, N. Kawamura, S. Ishiwata, M. G. Tucker, Y. Shimakawa, and J. P. Attfield, Nat. Commun. **2**, 347 (2011).

[30] M. Naka, H. Seo, and Y. Motome, Phys. Rev. Lett. **116**, 056402 (2016).

[31] S. Kojima, J. Nasu, and A. Koga, Phys. Rev. B **94**, 045103 (2016).

[32] I. Leonov, A. S. Belozerov, and S. L. Skornyakov, Phys. Rev. B **100**, 161112(R) (2019).

[33] M. Mizumaki, N. Ishimatsu, N. Kawamura, M. Azuma, Y. Shimakawa, M. Takano, and T. Uozumi, Phys. Rev. B **80,** 233104 (2009).

[34] A. Paul, A. Mukherjee, I. Dasgupta, A. Paramekanti, and T. Saha-Dasgupta, Phys. Rev. Lett. **122,** 016404 (2019).

[35] H. Raebiger, S. Lany, and A. Zunger, Nature (London) **453,** 763 (2008).

[36] J. P. Perdew, A. Ruzsinszky, G. I. Csonka, O. A. Vydrov, G. E. Scuseria, L. A. Constantin, X. Zhou, and K. Burke, Phys. Rev. Lett. **100,** 136406 (2008).

[37] X. Gonze, J.-M. Beuken, R. Caracas, F. Detraux, M. Fuchs, G.-M. Rignanese, L. Sindic, M. Verstraete, G. Zerah, F. Jollet, M. Torrent, A. Roy, M. Mikami, P. Ghosez, J.-Y. Raty, and D. Allan, Comput. Mater. Sci. **25,** 478 (2002).

[38] X. Gonze, Z. Kristallogr. Cryst. Mater. **220,** 558 (2005).

[39] M. Torrent, F. Jollet, F. Bottin, G. Zrah, and X. Gonze, Comput. Mater. Sci. **42,** 337 (2008).

[40] A. I. Liechtenstein, V. I. Anisimov, and J. Zaanen, Phys. Rev. B **52,** R5467 (1995).

[41] H. T. Stokes, D. M. Hatch, and B. J. Campbell, ISOTROPY Software Suite, https://iso.byu.edu.

[42] Y. Zhang, M. M. Schmitt, A. Mercy, J. Wang, and P. Ghosez, Phys. Rev. B **98,** 081108(R) (2018).

[43] X. Gonze, B. Seddon, J. A. Elliott, C. Tantardini, and A. V. Shapeev, J. Chem. Theory Comput. **18,** 6099 (2022).

[44] S. J. Carlsson, M. Azuma, Y. Shimakawa, M. Takano, A. Hewat, and J. P. Attfield, J. Solid State Chem. **181,** 611 (2008).

[45] J. Varignon, M. N. Grisolia, D. Preziosi, P. Ghosez, and M. Bibes, Phys. Rev. B **96,** 235106 (2017).

[46] S. Ishiwata, M. Azuma, M. Takano, E. Nishibori, M. Takata, M. Sakata, and K. Kato, J. Mater. Chem. **12,** 3733 (2002).

[47] C. M. Varma, Phys. Rev. Lett. **61,** 2713 (1988).

[48] P. Ghosez and J. Junquera, Annu. Rev. Condens. Matter Phys. **13,** 325 (2022).

[49] K. M. Rabe, Antiferroelectricity in oxides: A reexamination, in *Functional Metal Oxides* (John Wiley Sons, Ltd, New York, 2013), Chap. 7, pp. 221–244.

[50] S. E. Reyes-Lillo, K. F. Garrity, and K. M. Rabe, Phys. Rev. B **90,** 140103(R) (2014).

[51] Y. Qi and K. M. Rabe, Phys. Rev. B **106,** 125131 (2022).

[52] K. Yamauchi, T. Fukushima, and S. Picozzi, Phys. Rev. B **79,** 212404 (2009).

[53] M. Alexe, M. Ziese, D. Hesse, P. Esquinazi, K. Yamauchi, T. Fukushima, S. Picozzi, and U. Gsele, Adv. Mater. **21,** 4452 (2009).

[54] Nonadiabatic paths have been obtained fixing the atomic geometry to $\lambda = 0$ or $\lambda = 1$ and then constraining the electronic charge at each point to what it is along the adiabatic path, using constrained-DFT calculations.

[55] E. Bousquet, N. A. Spaldin, and K. T. Delaney, Phys. Rev. Lett. **106,** 107202 (2011).

[56] W. Yi, Y. Kumagai, N. A. Spaldin, Y. Matsushita, A. Sato, I. A. Presniakov, A. V. Sobolev, Y. S. Glazkova, and A. A. Belik, Inorg. Chem. **53,** 9800 (2014).

[57] J. B. Neaton, C. Ederer, U. V. Waghmare, N. A. Spaldin, and K. M. Rabe, Phys. Rev. B **71,** 014113 (2005).

[58] K. Oka, M. Azuma, W.-t. Chen, H. Yusa, A. A. Belik, E. Takayama-Muromachi, M. Mizumaki, N. Ishimatsu, N. Hiraoka, M. Tsujimoto, M. G. Tucker, J. P. Attfield, and Y. Shimakawa, J. Am. Chem. Soc. **132,** 9438 (2010).

[59] A. A. Belik, S. Y. Stefanovich, B. I. Lazoryak, and E. Takayama-Muromachi, Chem. Mater. **18,** 1964 (2006).

[60] N. Ikeda, H. Ohsumi, K. Ohwada, K. Ishii, T. Inami, K. Kakurai, Y. Murakami, K. Yoshii, S. Mori, Y. Horibe, and H. Kitô, Nature (London) **436,** 1136 (2005).

[61] K. Fujiwara, Y. Fukada, Y. Okuda, R. Seimiya, N. Ikeda, K. Yokoyama, H. Yu, S. Koshihara, and Y. Okimoto, Sci. Rep. **11,** 4277 (2021).

[62] S. Y. Park, K. M. Rabe, and J. B. Neaton, Proc. Natl. Acad. Sci. U.S.A. **116,** 23972 (2019).

[63] S. Y. Park, A. Kumar, and K. M. Rabe, Phys. Rev. Lett. **118,** 087602 (2017).